

Nonlinear electrical transport phenomena as fingerprints of a topological phase transition in ZrTe_5

Yusuff Adeyemi Salawu¹, Dilanath Adhikari¹, Jin Hee Kim², Jong-Soo Rhyee², Minoru Sasaki³, Ki-Seok Kim⁴✉ & Heon-Jung Kim^{1,5}✉

Topological phase transitions, influenced by magnetic fields, dopants, pressure, and temperature, create Berry curvature in band structures, challenging to detect due to resolution and scattering issues in spectroscopy and transport. Here, we propose nonlinear electrical transport phenomena as fingerprints of a topological phase transition in ZrTe_5 under magnetic fields. Both a nonlinear longitudinal conductivity $\Delta\sigma_L$ in a magnetic-field-aligned electric field and a third-order nonlinear Hall (transverse) conductivity $\Delta\sigma_{xy}$ in a magnetic-field-perpendicular electric field arise below a characteristic temperature T^* . The sensitivity of nonlinear transport to the band topology allows the detection of a subtle change in the band topology hidden in linear transport coefficients. Extending the previous scaling theory between linear transport coefficients (σ_{xx} and σ_{xy}), we also propose scaling relations for both linear (σ_{xx} and σ_{xy}) and nonlinear ($\Delta\sigma_L$ and $\Delta\sigma_{xy}$) transport coefficients. These scaling relations will help understand the interplay between the mechanisms of nonlinear transport coefficients and the influence of Berry curvature.

¹Department of Physics, Graduate School, Daegu University, Gyeongbuk, Republic of Korea. ²Department of Applied Physics and Institute of Natural Sciences, Kyung Hee University, Yong-In, Republic of Korea. ³Department of Physics, Faculty of Science, Yamagata University, Kojirakawa, Yamagata, Japan. ⁴Department of Physics, Pohang University of Science and Technology (POSTECH), Pohang, Gyeongbuk, Republic of Korea. ⁵Department of Materials-Energy Science and Engineering, College of Engineering, Daegu University, Gyeongbuk, Republic of Korea. ✉email: tkfd@postech.ac.kr; hjkim76@daegu.ac.kr

Berry curvature from a nontrivial band topology¹ is well established to play a central role in both the anomalous Hall coefficient^{2,3} and negative longitudinal magnetoresistance (LMR) in a Weyl metallic state^{4–9}. For instance, an LMR, originating from the nontrivial topological structure of the chiral anomaly^{10–14}, i.e., non-conservation of chiral charges, in a Weyl band induced by an external magnetic field was measured in Dirac and Weyl metals. However, various disorder scattering channels are also well known to cause similar effects on these linear transport coefficients^{15–17}, which hinders the understanding of the nontrivial band topology based on the linear transport coefficients. In this respect, considering nonlinear transverse and longitudinal transport coefficients as measures for the appearance of the Berry curvature associated with a topological phase transition (TPT) of an electronic band structure is natural. The present experiments suggest that such nonlinear transport coefficients are more sensitive in verifying a TPT than linear coefficients, reflecting the nature of the electronic wavefunctions.

Recently, various kinds of nonlinear transport coefficients have been proposed, which are classified by intraband scattering^{18,19} and interband transition^{20,21} mechanisms in the presence of Berry curvature. Specifically, the Berry curvature dipole^{22–24}, Berry-connection polarizability (BCP) tensor^{25,26}, and quantum geometric tensor^{27,28} are responsible for nonlinear transport coefficients. Some of them were measured^{26,27}. The nonlinear electrical transport resulting from these quantities has been contrasted with the electrical nonlinearity caused by the opening of a ballistic channel. Despite these recent developments, the present study shows that all these proposed mechanisms for nonlinear transport coefficients cannot explain our experimental results that confirm the existence of a TPT in ZrTe₅.

Here, we investigate the nonlinear electrical transport phenomena of ZrTe₅, which has an orthorhombic layered structure with space group Cmc_{2h} (D_{2h}^{17})^{2,29,30}. For our purpose, ZrTe₅, a topological metal with a TPT, is an appropriate system. Because the present ZrTe₅ is not sufficiently clean, it will not show ballistic conduction and the resultant nonlinearity^{31,32}. Along with a nonlinear longitudinal conductivity $\Delta\sigma_L$ for $E \parallel B$, which violates Ohm's law, we uncover a nonlinear Hall conductivity $\Delta\sigma_{xy}$ quadratic in the applied current for $E \perp B$. This result is consistent with the presence of inversion symmetry. Both $\Delta\sigma_L$ and $\Delta\sigma_{xy}$ arise at the same temperature $T^* \sim 30$ K, and their emergence is intimately related to the TPT known to occur in the vicinity of the resistivity peak temperature. Remarkably, T^* is the 'transition temperature' of the TPT, which is revealed by $\Delta\sigma_L$ and $\Delta\sigma_{xy}$ but hidden in linear transport coefficients. In addition, the (linear) longitudinal conductivity σ_{xx} , the (linear) Hall conductivity σ_{xy} , $\Delta\sigma_{xy}$ for $E \perp B$, and $\Delta\sigma_L$ for $E \parallel B$ are found to show scaling relations. In particular, $\sigma_{\text{AHE}} \sim \sigma_{xx}$ suggests skew scattering as a dominant mechanism of the anomalous Hall effect (AHE) in ZrTe₅. A scaling relation of $\Delta\sigma_L \sim (\sigma_{\text{AHE}})^3$ and a crossover from $\Delta\sigma_{xy} \sim \Delta\sigma_L$ to $\Delta\sigma_{xy} \sim (\Delta\sigma_L)^2$ are also observed, which manifest the underlying mechanism of the nonlinear Hall effect in ZrTe₅. These extended scaling relations provide a framework to understand the interplay between a nontrivial band topology and disorder scattering as the conventional conductivity scaling laws do. The AHE, usually observed in ferromagnetic metals, is more 'anomalous' in nonmagnetic ZrTe₅, and it cannot be understood within existing Weyl metal frameworks. This AHE resembles the three dimensional (3D) quantum Hall effect reported in ZrTe₅³³. However, a later study ruled out this possibility by confirming that the charge density wave, which is requisite for the 3D quantum Hall effect, is absent in ZrTe₅³⁴. This AHE with unknown origin implies an elusive ground state of

ZrTe₅. The nature of the AHE also changes at T^* , as discussed below.

The topological nature of ZrTe₅ remains controversial because of its sensitivity to the details of the lattice parameters and the purity of the crystals. Some angle-resolved photoemission spectroscopy (ARPES)¹¹ and transport^{11,35} studies have suggested a 3D Dirac metallic state with no finite gap. This picture was also supported by an infrared (IR) spectroscopy³⁶, magneto-optical³⁷, and other transport³⁸ measurements. In contrast, two scanning tunnelling microscopy (STM)^{39,40} and laser-based ARPES⁴¹ studies concluded that ZrTe₅ is a weak topological insulator (TI). In addition, other ARPES and STM studies detected a metallic surface state, which indicates that ZrTe₅ is a strong TI^{42,43}. This contradictory situation changed when a TPT between a strong TI and a weak TI with an intermediate Dirac metallic region was observed^{44,45}. A pronounced peak in the temperature dependence of the resistivity indirectly signifies the intermediate Dirac metallic state. An IR spectroscopy study found that the energy gap closes around the peak temperature, where the optical response exhibits the characteristic signatures of a Dirac metallic state⁴⁴. A nuclear magnetic resonance (NMR) study also demonstrated temperature-dependent topological characteristics with an intermediate TPT, whose transition temperature was found to be lower than the peak temperature⁴⁵. However, unlike the IR spectroscopy study, this NMR study suggested a weak TI at low temperatures. Despite the ambiguity about the topological nature below and above the peak region, the peak region was identified as corresponding to a Dirac metallic state. This identification offers a chance to observe phenomena related to a Dirac metal with an intermediate TPT. This peak appears at a relatively high temperature (~ 130 K) and at a lower temperature in the crystals grown by the chemical vapour transport (CVT) and flux methods, respectively. Thus, the Dirac metallic state may be a ground state in flux-grown crystals. This study investigates flux-grown crystals, whose resistivity peak is at $T = 40$ K but whose high resistivity extends down to $T = 0$ K. Negative LMR originating in the chiral anomaly²⁹ and the AHE from the Berry curvature were observed in flux-grown ZrTe₅^{2,46–48}, supporting the Dirac and Weyl metallicity. The band structure of ZrTe₅ in the Dirac metallic state is simple, as revealed by ARPES^{36,40,49}. A single Dirac band exists at Γ in reciprocal space [Fig. 1a], and the Fermi energy crosses near the nodal point. In this study, we optimized the growth conditions of ZrTe₅ single crystals to produce crystals that exhibit pronounced topological properties, such as the AHE and negative LMR.

Results

Basic characterization of topological semimetal ZrTe₅ grown.

Using the Te-flux method, we grew 13 single crystals (S1–S13) with different heating profiles and characterized them [see Supplementary Fig. 1 and Supplementary Table 1]^{11,50,51}. Among these single crystals, only three samples (S11, S12, and S13) with low carrier density and large residual resistivity exhibit very pronounced AHE and negative LMR. These results indicate that the Fermi energy position of these particular samples is close enough to the nodal point to reveal topological properties, as shown in Fig. 1a. Hall effect, magnetoresistance (MR), and current (I)-voltage (V) measurements were conducted in the six-probe configuration, where the longitudinal (ρ_{xx}) and transverse (ρ_{xy}) resistivities can be simultaneously measured. We tested three different magnetic field B and current I (or E) configurations for the I - V measurements: transverse ($B \perp E$, B is out of plane), longitudinal ($B \parallel E$), and in-plane Hall ($B \perp E$, B is in the plane) configurations.

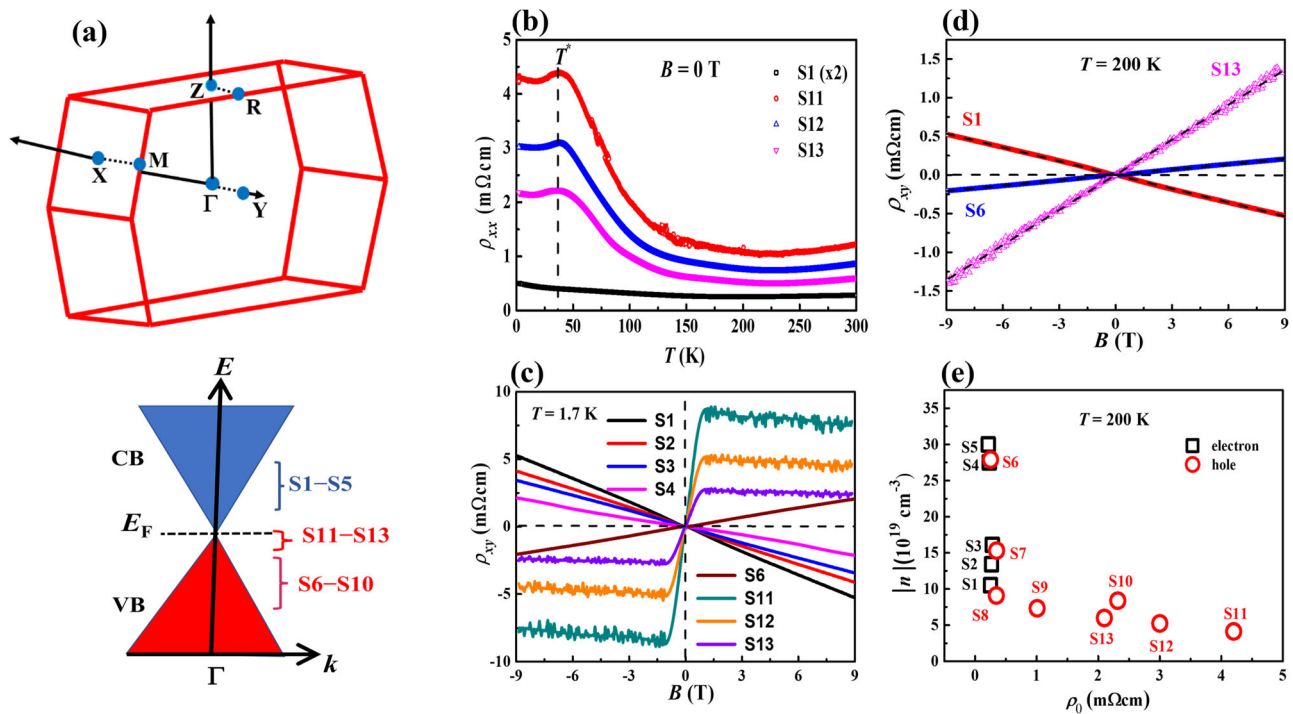


Fig. 1 Electronic structure and basic characterization of topological semimetal ZrTe₅ grown under different conditions. **a** Schematic band structures and Brillouin zones of ZrTe₅. The Dirac band appears at the Γ point^{38,46–48,50,63}. The positions of the Fermi energy for the S1–S13 samples are shown along with a schematic diagram of the Dirac band. **b** Temperature dependence of the resistivity for four ZrTe₅ single crystals (S11, S12, S13, and S1) grown under different conditions. In particular, the three ‘insulating’ samples (S11, S12, S13) show a characteristic peak at approximately 40 K. This peak is a precursor of the topological phase transition at $T^* \sim 30$ K. **c** Field dependence of the Hall resistivity $\rho_{xy}(B)$ for several ZrTe₅ single crystals grown under different conditions. All measurements were performed at $T = 1.7$ K. The origin of the step-like $\rho_{xy}(B)$ is still elusive^{2,11,47}. **d** Hall resistivity $\rho_{xy}(B)$ for S11, S6, and S1 samples at $T = 200$ K. The anomalous Hall effect is absent above 80 K. The dashed lines fit the experimental data to a linear function. **e** Absolute value of carrier density n estimated at $T = 200$ K as a function of residual resistivity ρ_0 at $T = 1.7$ K. The samples that show the AHE and negative LMR have small $|n|$ and large ρ_0 .

Figure 1b presents the temperature dependence of the resistivity for the S1, S11, S12, and S13 samples. Compared to the S1–S10 samples, S11, S12, and S13 have a more pronounced insulating behaviour with a relatively large residual resistivity ρ_0 [Supplementary Fig. 2a, b]. Even though the values of ρ_0 are large, they are still on the order of a few m Ω cm for S11, S12, and S13. The relatively large ρ_0 is correlated with a pronounced AHE at $T = 1.7$ K, as shown in Fig. 1c and Supplementary Fig. 2c. While the Hall resistivity is linear in B for S1–S10, a pronounced step occurs at low B for S11, S12, and S13. This step is a signature of the AHE, as reported in previous studies^{2,47}. How such shape and magnitude of anomalous Hall signals emerge in the nonmagnetic metal ZrTe₅ needs to be understood. As previously noted², ferromagnetism plays no role here because of its absence. The Hall resistivity in the Dirac metal should be linear in B because the separation between two nodal points, which determines the Hall resistivity, is proportional to B . However, this is not the case here, which suggests the essential roles of exotic mechanisms for the AHE in ZrTe₅. Relatively large ρ_0 and the occurrence of the AHE are connected with a low carrier density. We analysed the Hall resistivity at $T = 200$ K to estimate the carrier density, as illustrated in Fig. 1d [Supplementary Fig. 2d]. We selected $T = 200$ K because the S11, S12, and S13 samples show the AHE at low temperatures. The S11, S12, and S13 samples have the smallest carrier density n at $T = 200$ K among the S1–S13 samples. Consequently, these three samples are located at the lower-right corner of the $|n|$ – ρ_0 plane, as shown in Fig. 1e. In a previous study, the researchers argued that charge puddles significantly affect their low-carrier-density ZrTe₅ samples²⁹. Our

system also displays low carrier density, but at $\sim 10^{19}$ cm⁻³, it is notably higher than the $\sim 10^{16}$ cm⁻³ density reported in the previous report. This likely leads to a less substantial influence of charge puddles on our sample, as the higher carrier density suppresses the formation of charge inhomogeneities.

In S11, S12, and S13, we observe a negative LMR. Supplementary Fig. 3a displays the LMR at $T = 1.7$ K. A dip exists near $B = 0$ T, which was attributed to a weak antilocalization effect in a previous study^{12,52}. Outside the dip region, the MR decreases with increasing B . Interestingly, the magnitude of the negative LMR at $B = +9$ T scales well with ρ_0 and the magnitude of the anomalous Hall conductivity σ_{AHE} at $B = +9$ T [Supplementary Fig. 3b]. To determine the temperature at which the negative LMR and anomalous Hall conductivity vanish, we measured the LMR and anomalous Hall conductivity at different temperatures. At low temperatures, the MR is negative. With increasing temperature, the MR undergoes a sign change. A crossover from a negative MR to a positive MR occurs at approximately 80 K. Similarly, a very pronounced σ_{AHE} is observed at low temperatures, reaching $3 \text{ k}\Omega^{-1} \text{ cm}^{-1}$ at $T = 1.7$ K for the S11 sample. With increasing temperature, σ_{AHE} decreases and eventually vanishes above approximately 80 K. To quantify the magnitude of the negative LMR, we analysed the negative LMR based on the weak-field conductivity formula for a Weyl metal¹². In this formula, the B dependence of the conductivity $\sigma_L(B)$ is given by $\sigma_L(B) = (1 + C_W B^2) \cdot \sigma_{\text{WAL}}$. Here, C_W is a correction factor for a negative LMR due to the chiral anomaly, and σ_{WAL} is the conductivity with weak antilocalization correction. The conductivity from other electron

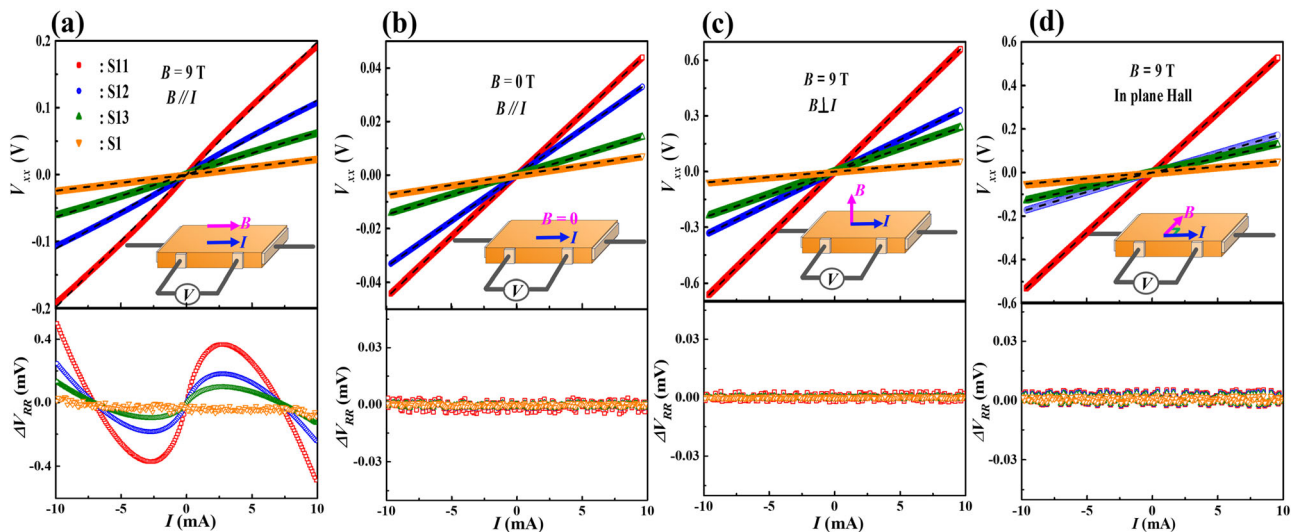


Fig. 2 Current-voltage measurements in different experimental configurations. **a–d** Voltage V as a function of current I at $T = 1.7$ K in the longitudinal configuration ($B // I$) at $B = 9$ T, at $B = 0$ T, in the transverse configuration ($B \perp I$) at $B = 9$ T, and in the in-plane Hall configuration at $B = 9$ T, respectively, and corresponding regular residual data obtained by subtraction of a linear slope for four different samples S11, S12, S13, and S1. The current-voltage curve is nonlinear only in the longitudinal configuration. The corresponding insets show a schematic diagram of the experimental setup.

or hole carriers σ_n is absent due to their nonexistence in ZrTe_5 , which is supported by the band structure^{47,48,50}. As expected, C_W decreases with increasing temperature, reaching a zero value at approximately 80 K [Supplementary Fig. 3c–e]. The value of σ_{AHE} at $B = -9$ T also becomes zero near the same temperature [Supplementary Fig. 3f–h], suggesting a strong correlation between the negative LMR and the AHE [see Supplementary Note 1 for more details].

Current-voltage measurements in different experimental configurations. Figure 2 presents the I - V characteristic curves obtained in four different configurations for the S1, S11, S12, and S13 samples. The most remarkable curves are those obtained in the longitudinal configuration with $B = +9$ T ($E // B$), in which the I - V curves become nonlinear for the S11, S12, and S13 samples. The deviation from linearity implies a violation of Ohm's law^{10,53}, which is impossible in a conventional metallic system. The nonlinearity can be more clearly seen in the difference curve between the data and the linear fitting (the regular residual of the voltage ΔV_{RR} as shown in Fig. 2). Remarkably, a systemic structure, which would not exist if it were due to random errors, is present in this difference curve for the S11, S12, and S13 samples. In contrast, no such structure is detected for the S1 sample. These results suggest that the nonlinearity is genuine, and the AHE, negative LMR, and nonlinear I - V curves share a common origin, i.e., the existence of Weyl nodes. The presence of nonlinear I - V curves is intimately related to the condition of $E // B$ for the S11, S12, and S13 samples. In all the conditions other than $E // B$ that we investigated ($B = 0$, $E \perp B$, and in-plane Hall configurations), the I - V curves are strictly linear, and the difference curve has no apparent structure. We effectively eliminated the heating effect, as demonstrated in Supplementary Fig. 4 and Supplementary Fig. 5, and established low-resistance contacts with the samples, evidenced by Supplementary Fig. 6. These measures were crucial in further confirming the authenticity of the observed nonlinearity. It is crucial to note that our samples fall within the so-called “dirty” limit, as the lack of Shubnikov-de Haas oscillations indicates. This is consistent with our observed negative LMR, and violation of Ohm's law found in these samples. These phenomena can be understood within the scope of the quasi-classical Boltzmann transport theory, as described in

references^{10,54}. This theory implies that the system operates in a quasi-classical regime, where Landau quantization is smeared out due to disorder. The ‘dirtiness’ of our samples should not be interpreted as poor quality but rather an indication of a specific charge transport regime induced by a high level of disorder.

Field-temperature dependence of the nonlinear conductivity.

Next, we examined the field and temperature dependence of the nonlinear I - V curves. The deviation ΔI from the linear curve with a slope at $V = 0$ was defined to quantify the magnitude of the nonlinearity for the S11 sample, as shown in Fig. 3c, d. In the longitudinal configuration ($E // B$) [Fig. 3a], ΔI becomes larger overall with increasing B and decreasing T . Notably, the nonzero ΔI persists up to $T^* \sim 30$ K, which is a slightly higher temperature than that in the case of $\text{Bi}_{1-x}\text{Sb}_x$ ($x = 3\text{--}4\%$)^{10,53}. Remarkably, T^* is quite close to the peak temperature in the temperature dependence of the resistivity^{44,45}. As the TPT with an intermediate Dirac metallic state was reported to reside near this peak temperature, T^* is identified as the ‘transition temperature’ of the TPT. Nevertheless, the precise nature of the phase transition in ZrTe_5 is still a matter of ongoing debate. Some evidence points towards a transition from a weak TI to a Dirac metal state^{44,45}, while other studies propose the transition stem from a trivial insulator or strong TI state^{42,43}. Unfortunately, our experimental setup does not allow a definitive determination of the initial state, which would likely require more advanced spectroscopic techniques. From the nonlinear I - V curves, we calculated the nonlinear longitudinal conductivity $\Delta\sigma_L$ as a function of the voltage V . $\Delta\sigma_L(V)$ is found to be quadratic in V , as Boltzmann transport theory predicts^{10,54}. As with ΔI , $\Delta\sigma_L$ increases overall with increasing B [Fig. 3e] and decreasing T [Fig. 3f]. The B dependence of $\Delta\sigma_L$ is well described by the formula $\Delta\sigma_L = b_2(B) \cdot E^2$, with $b_2(B) = C^{(2)}B^2 + C^{(1)}B^4$. This experimental result is in perfect agreement with the previous results [10], ensuring the validity of Fig. 3g. The temperature dependence of $\Delta\sigma_L$ was also investigated, as shown in Fig. 3h, and $b_2(T)$ vanishes at $T^* \sim 30$ K. $b_2(T)$ is well described by the formula $b_2(T) = b_2(0) \cdot [1 - (T/T^*)^t]$, where $b_2(0)$ is a coefficient and t is the characteristic exponent [$t = 1.2$]. The T^* extracted is consistent with the temperature at which b_2 vanishes. Our ZrTe_5 samples, which undergo a transition

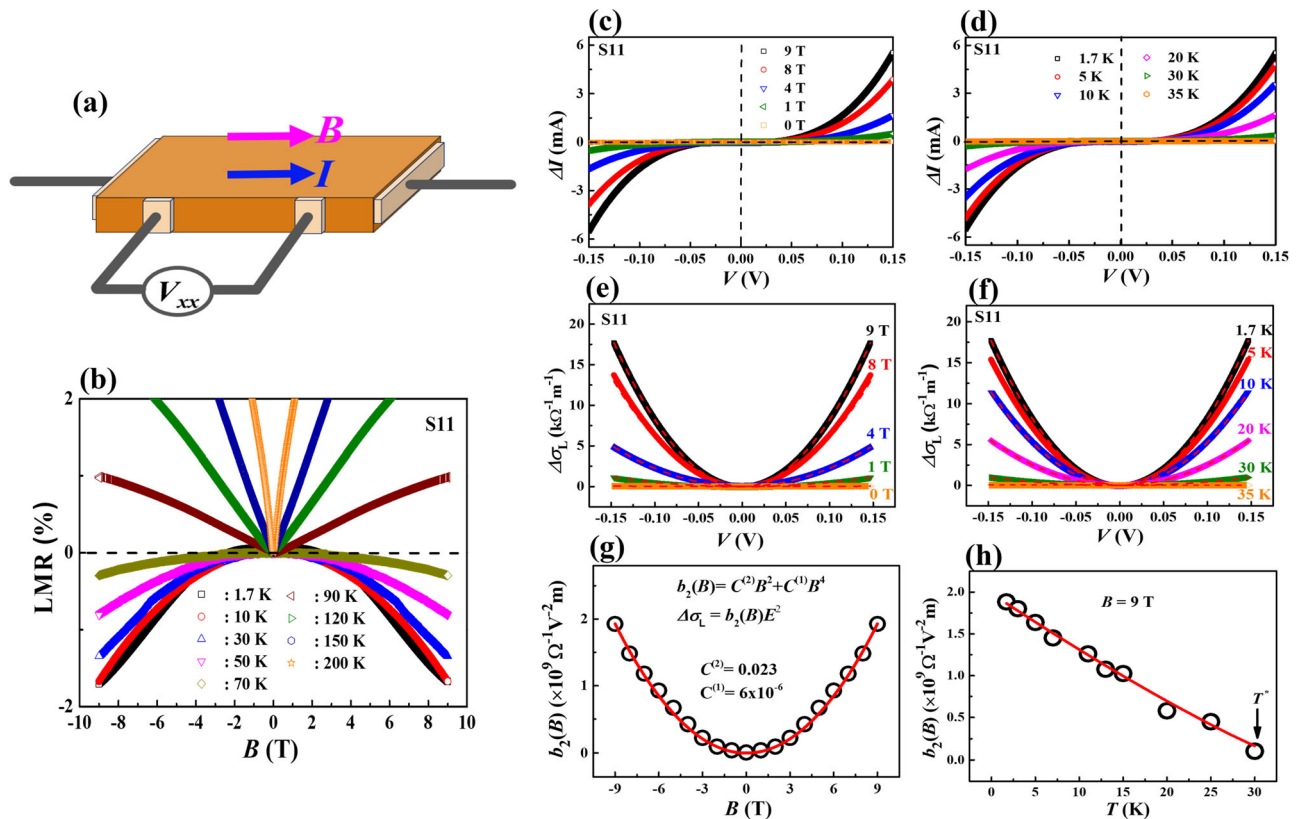


Fig. 3 Negative longitudinal magnetoresistance and field/temperature dependence of the nonlinear conductivity. **a** Schematic diagram of the longitudinal experiment ($B//I$). **b** Longitudinal magnetoresistance (LMR) measurement for sample S11 at different temperatures. Here, the MR is defined as $[\rho(B) - \rho(0)]/\rho(0) \times 100$. The negative MR turns into a positive MR at approximately 80 K. **c, d** ΔI curves obtained by subtraction of a linear slope in different magnetic fields B at $T = 1.7$ K and at different temperatures at $B = 9$ T, respectively. ΔI is a measure of the nonlinearity. **e, f** Nonlinear longitudinal conductivity $\Delta\sigma_L$ as a function of voltage at different magnetic fields B and temperatures T , respectively. The quadratic dependence of $\Delta\sigma_L$ on the voltage is consistent with theoretical calculations based on the Boltzmann transport equation^{10,54}. **g** B dependence of b_2 extracted from the conductivity curves in **e**. b_2 follows the relation $b_2(B) = C^{(2)}B^2 + C^{(1)}B^4$, which is also in agreement with the Boltzmann transport approach^{10,54}. **h** Temperature dependence of b_2 extracted from the conductivity curves in **f**. b_2 vanishes at $T^* \sim 30$ K.

around 30 K, display low carrier densities [see Supplementary Note 2, Supplementary Figs. 7–10 for more details]. However, our observations of linear I - V curves in the E and B configurations other than $E//B$ imply a persisting metallic state. Moreover, there are ARPES results confirming the presence of Fermi surfaces for the samples whose properties are similar to ours⁴².

Field-temperature dependence of the nonlinear Hall effect.

Now, we discuss the nonlinear Hall voltages V_{xy} probed for $E \perp B$ [Fig. 4a]. At a low electric field, we first measured the B dependence of V_{xx} and V_{xy} and converted it into that of σ_{xx} and σ_{AHE} [Fig. 4b]. Unexpectedly, we observe that the V_{xy} signals are nonlinear in the electric current. Here, we present ΔV_{xy} , in which the part linear in the current has been subtracted. As shown in Fig. 4c, ΔV_{xy} is substantial at high currents. We rule out the heating effect as the origin of the nonlinearity in ΔV_{xy} because the nonlinearity is absent at $B = 0$. ΔV_{xy} systematically varies with B , but unusually, the values at $B = +9$ T and -9 T are different. This is because ΔV_{xy} contains signals both symmetric and antisymmetric with respect to B . If ΔV_{xy} is a ‘Hall’ signal, then it should be antisymmetric. Thus, we consider the possibility that ΔV_{xy} is contaminated by the symmetric signals resulting from $\Delta\sigma_L$ due to the slight misalignment of the contacts and the B direction. We antisymmetrize ΔV_{xy} to remove the symmetric component and obtain the antisymmetric component ΔV_{xy}^A . We find $\Delta V_{xy}^A = \alpha \cdot I^3$. α is almost linear in B , as shown in Fig. 4e, and

vanishes around $T^* \sim 30$ K, where $\Delta\sigma_L$ also vanishes even though α is small above 20 K [Fig. 4f]. Using the nonlinear Hall voltage ΔV_{xy}^A and the resistivity-to-conductivity conversion method, we calculate $\Delta\sigma_{xy}$ and find that it follows $\Delta\sigma_{xy} = \beta \cdot I^2$ [see Supplementary Note 3]. A second-order nonlinear Hall effect was reported^{18,22,55–57}, which follows the relation $J_\alpha = \chi_{\alpha\beta\gamma} E_\beta E_\gamma$, where J_α , E_β , and $\chi_{\alpha\beta\gamma}$ are the current in the α direction, electric field in the β direction, and nonlinear conductivity tensor, respectively. This second-order nonlinear Hall effect, originating from the Berry curvature dipole and observed in a system with broken inversion symmetry at $B = 0$, gives rise to a nonlinear Hall voltage quadratic in E . The ΔV_{xy}^A that we observe is therefore not the signal from this second-order nonlinear Hall effect as shown in Supplementary Fig. 11 due to the third-order nature of ΔV_{xy}^A , i.e., $\Delta V_{xy}^A = \alpha \cdot I^3$. This third-order nonlinear Hall effect is also observed in AC transport experiments [Supplementary Fig. 12 and Supplementary Note 4]. These observations are consistent with the presence of inversion symmetry within our system. The third-order nature of the effect aligns with our understanding that the $ZrTe_5$ studied here is a centrosymmetric system. This consistency corroborates our experimental findings and the theoretical expectations for such a system.

Scaling relations among linear and nonlinear conductivities. For ferromagnetic metals that exhibit the AHE, three different

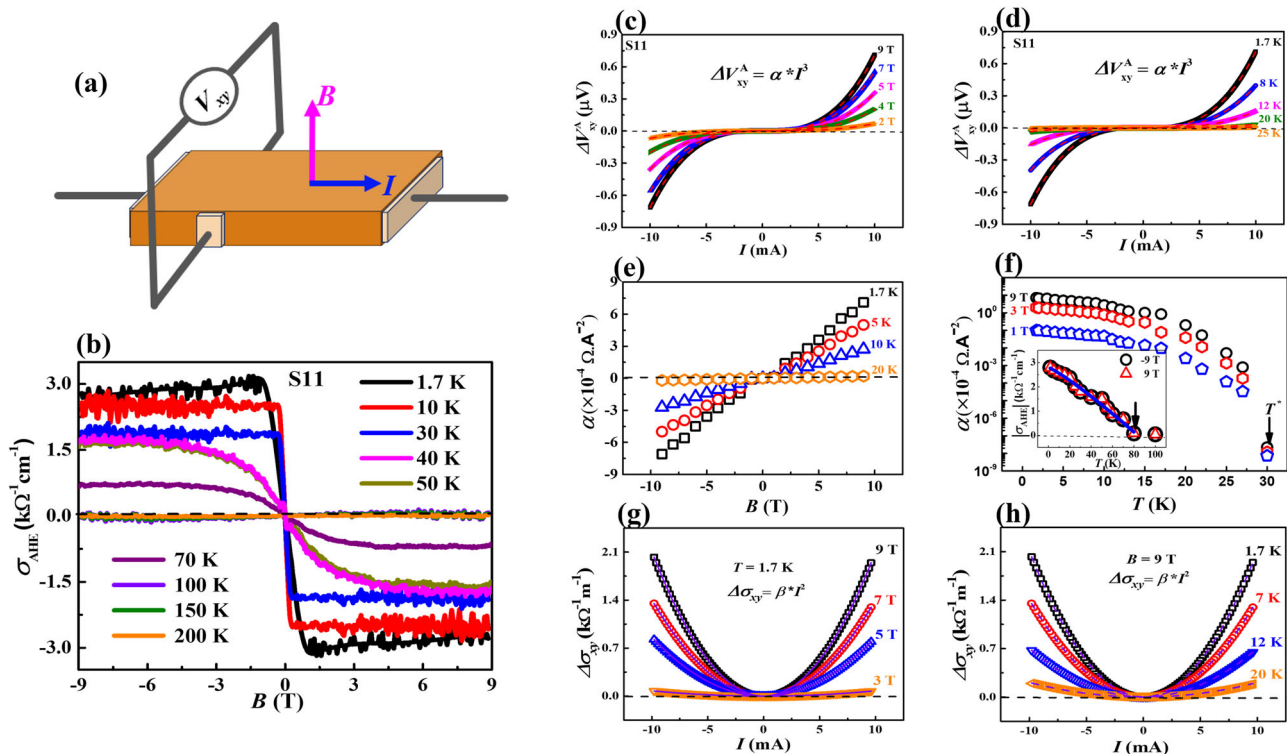


Fig. 4 Anomalous Hall conductivity and field/temperature dependence of the nonlinear Hall effect. **a** Schematic diagram of the transverse configuration ($B \perp I$). **b** Anomalous Hall conductivity for the S11 sample at different temperatures. The nature of the curves changes at $T^* \sim 30$ K. **c, d** Antisymmetrized nonlinear Hall voltage ΔV_{xy}^A . These curves are obtained by subtracting the linear component and then performing antisymmetrization. The dotted curve is a fit based on $\Delta V_{xy}^A = \alpha I^3$. **e, f** Coefficient α obtained from the fit of **c, d** as a function of magnetic field B and temperature T , respectively. **g, h** Nonlinear Hall conductance $\Delta\sigma_{xy}$ as a function of the applied current at different magnetic fields B and temperatures T , respectively. Both α and $\Delta\sigma_{xy}$ vanish at $T^* \sim 30$ K.

scaling regimes exist between σ_{xy} and σ_{xx} depending on their mechanisms: $\sigma_{xy} \sim (\sigma_{xx})^{1.6}$, $\sigma_{xy} \sim \text{const.}$, and $\sigma_{xy} \sim \sigma_{xx}^{58-60}$. The first relationship holds when the side jump is dominant. In contrast, the last regime occurs when skew scattering is the main factor in the super clean limit. A constant σ_{xy} implies that the Berry curvature governs the AHE. To understand the underlying mechanism for the AHE of ZrTe_5 , we derived the scaling relation between σ_{AHE} and σ_{xx} . The scaling relationship in a log-log plot is displayed in Fig. 5a, where interesting structures exist, with a linear scaling curve in the upper part and three parallel lines with an exponent of ~ 3 in the lower part. The former curve is composed of the low-temperature data ($T = 1.7$ K, 10 K, and 30 K), where the $\sigma_{\text{AHE}}(B)$ curve shows an abrupt step near $B = 0$ T. In contrast, the three parallel lines present below this scaling curve consist of the high-temperature data ($T = 40$ K, 50 K, and 70 K). At these high temperatures, $\sigma_{\text{AHE}}(B)$ is more rounded compared to low temperature $\sigma_{\text{AHE}}(B)$ [Fig. 4b]. The different exponents in the scaling relations indicate different mechanisms for the AHE in ZrTe_5 at different temperatures. The scaling exponent of ~ 1 suggests that ZrTe_5 belongs to the skew-scattering-dominant region [Fig. 5b]. In contrast, the scaling exponent of ~ 3 has not yet been reported. However, regardless of the exponent value, the entire scaling curves for the S11-S13 samples are located in the intrinsic region of the phase diagram because of low σ_{xx} values. This discrepancy may be due to the inapplicability of the frameworks developed for ferromagnetic metals to nonmagnetic topological metals such as ZrTe_5 .

In the skew-scattering region [$\sigma_{\text{AHE}} \sim \sigma_{xx}$], other scaling relations are uncovered. The first is the scaling relation between the nonlinear transport coefficient $b_2(B)$ (or $\Delta\sigma_L$) and σ_{AHE} . Figure 5c shows a linear scaling curve with a slope of ~ 3 in the log-log plot between $b_2(B)$ and σ_{AHE} . This linearity, which implies

a power-law behaviour with an exponent of ~ 3 , holds in a given sample and among different samples. Additionally, all the curves at different B are scaled into a single universal curve when b_2 is divided by $B^{2.8}$ [Fig. 5c]. Thus, all these scaling analyses suggest $b_2(B) \sim (\sigma_{\text{AHE}})^3 B^{2.8}$. This scaling relation between $b_2(B)$ and σ_{AHE} has not been previously observed. While σ_{AHE} is a property of both the Fermi sphere and Fermi surface caused by nonzero Berry curvature⁶¹, $\Delta\sigma_L$ is solely a contribution of the Fermi surface originating from the chiral anomaly according to the previous results¹⁰. Moreover, while σ_{AHE} is given by the second-order current-current correlation function $\sim \langle j^2 \rangle$, where j is the current density, $b_2(B)$ is given by the fourth-order current-current-current-current correlation function $\sim \langle j^4 \rangle$. Thus, the scaling relation of $b_2(B) \sim (\sigma_{\text{AHE}})^3$ indicates that naive dimensional analysis does not work.

We also found another interesting scaling relation between $\Delta\sigma_{xy}$ and $\Delta\sigma_L$ at a given voltage, as presented in Fig. 5d [Supplementary Fig. 13]. It also occurs in the skew-scattering region [$\sigma_{\text{AHE}} \sim \sigma_{xx}$]. The slope of this log-log plot changes from ~ 1 at low $\Delta\sigma_L$ to ~ 2 at high $\Delta\sigma_L$, suggesting that different scaling regions may exist. The lower slope at low $\Delta\sigma_L$ indicates that the naive dimensional analysis holds, distinct from the scaling relation of $b_2 \sim (\sigma_{\text{AHE}})^3$. In contrast, the higher slope suggests that this simple picture breaks down. At different voltages, the observed curve shapes are similar [Supplementary Fig. 3]. Along with $b_2(B) \sim (\sigma_{\text{AHE}})^3$, this scaling relation with a crossover extends the scaling law of the AHE from the linear to nonlinear regime. The linear scaling law between σ_{AHE} and σ_{xx} has been a guideline to interpret the linear AHE. Likewise, the extended scaling relations provide a framework to understand the mechanisms of nonlinear transport coefficients and the influence of Berry curvature. The implication of the nonlinear relation with

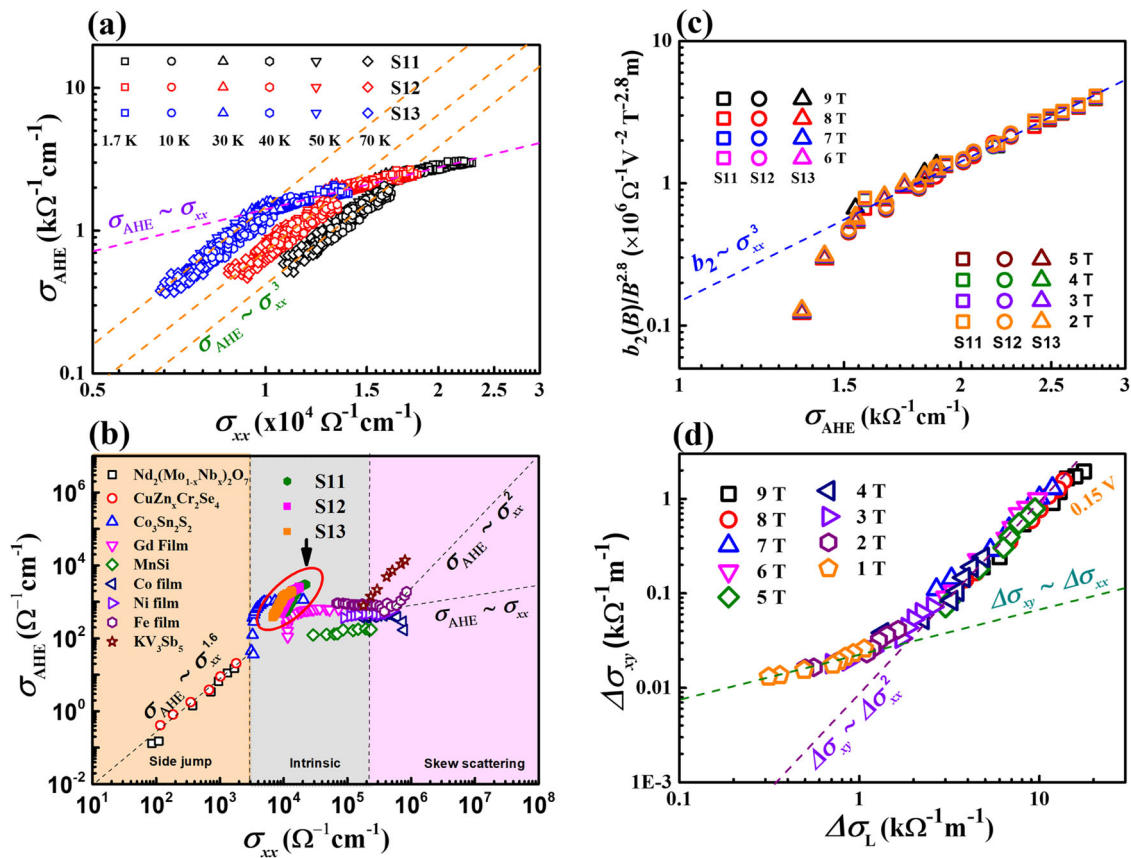


Fig. 5 Scaling relations among linear and nonlinear conductivities. **a** σ_{AHE} versus σ_{xx} for the S11, S12 and S13 samples in log-log plot. The upper curve shows an exponent of -1 , and the three lower curves exhibit an exponent of -3 . The exponent of -1 , which occurs below $T^* \sim 30$ K, implies that the samples are in the skew-scattering region, whereas the scaling region between 40 K and 70 K, has not yet been reported in the conductivity scaling of ferromagnetic metals. **b** σ_{AHE} versus σ_{xx} for a variety of materials^{58,60,64–66} spanning the various anomalous Hall effect regimes from the side-jump regime to the intrinsic and skew-scattering regimes. Regardless of the exponent value, all the scaling curves for the S11, S12, and S13 samples reside in the intrinsic region of the phase diagram because of low σ_{xx} values. The discrepancy between the exponent value and the region of the scaling law is not well understood, and the origin of σ_{AHE} has not been clarified. **c** Scaling relation between b_2 and anomalous Hall conductivity σ_{AHE} . b_2 follows $b_2 \sim (\sigma_{\text{AHE}})^3$. While the scaling for the linear conductivities (σ_{AHE} and σ_{xx}) holds below ~ 80 K, this nonlinear scaling curve holds below $T^* \sim 30$ K. This nonlinear scaling may be a property of the skew-scattering region below $T^* \sim 30$ K. **d** A scaling relation exists between $\Delta\sigma_L$ and $\Delta\sigma_{xy}$ at a given voltage and below $T^* \sim 30$ K. This scaling curve undergoes a crossover from the region of an exponent of one at low conductivities (high temperatures) [$\Delta\sigma_{xy} \sim \Delta\sigma_L$] to the region of an exponent of two at high conductivities (low temperatures) [$\Delta\sigma_{xy} \sim (\Delta\sigma_L)^2$]. While simple dimensional analysis applies to the low conductivity region [$\Delta\sigma_{xy} \sim \Delta\sigma_L$], it cannot explain the scaling relation at high conductivities [$\Delta\sigma_{xy} \sim (\Delta\sigma_L)^2$].

a crossover is the existence of another scaling region that divides the skew-scattering region. At high temperatures in the skew-scattering region, where $\Delta\sigma_{xy}$ and $\Delta\sigma_L$ are small, simple dimensional analysis applies for both nonlinear scaling relations. Therefore, the region of importance is the new low temperature region where $\Delta\sigma_{xy} \sim (\Delta\sigma_L)^2$ is satisfied [see Supplementary Note 5 for more details]. To clarify the nature of this region, further theoretical studies are needed.

Discussion

The observation of nonlinear electrical responses, such as the violation of Ohm's law and the third-order nonlinear Hall effect, in ZrTe_5 is quite surprising because such responses are believed to be impossible in metals in the diffusive limit. Without a nontrivial band topology, this would not occur in ZrTe_5 . For the $E // B$ configuration, a finite difference in the Fermi energy of $2\mu_5$ is developed owing to the chiral anomaly. The carriers corresponding to the $2\mu_5$ range respond to the external perturbations E and B . This situation drastically differs from the metals with a trivial band topology, where only a tiny fraction of carriers at the Fermi energy reacts to the perturbations. This is why the violation

of Ohm's law is present in the Weyl metallic state realized for $E // B$. The Boltzmann transport theory that considers the above mechanism successfully described the experimental results⁵⁴. Thus, the present result implies that Ohm's law can be violated in other Weyl and topological metals with similar band topologies. However, the Weyl metal picture cannot explain all the experimental results in the present study. First, the presence of the ΔV_{xy}^A signals in the transverse configuration ($B \perp E$) cannot be elucidated by the chiral anomaly effect because of the perpendicular field configuration. One possible origin is the recently reported third-order nonlinear Hall effect²⁶. This Hall effect results from the BCP tensor^{19,25,26}. BCP is an intrinsic band geometric quantity that characterizes the positional shift of Bloch electrons under applied E and B fields. It should be strongly enhanced in small gap regions, especially band degeneracies. Phenomenologically, ΔV_{xy}^A proportional to I^3 (or E^3) is consistent with the third-order nature expected by the BCP scenario. However, the possibility that BCP alone can fully explain the finite ΔV_{xy}^A at $B \neq 0$ is unlikely. It cannot explain $\Delta\sigma_L$ below $T^* \sim 30$ K. Irrespective of the BCP scenario as a relevant one for the third-order nonlinear Hall effect in ZrTe_5 , one notable point is the possible

change in the band topology at T^* , which is not detected in the linear transport coefficients. This may be because nonlinear conductivities are more sensitive to changes in the band topology, such as the Berry curvature dipole, BCP, and chiral anomaly, reflecting the nature of the wavefunctions. Another possible origin of nonlinear conductivities is ballistic conduction^{29,62}. However, this scenario is not relevant to the present case, as previously discussed. While the scaling laws among different linear and nonlinear conductivities suggest essential influences of the non-trivial band topology on these conductivities, the origin of the nonlinear Hall conductivity still needs to be completely understood. Thus, this calls for further theoretical and experimental studies that can reveal a solid connection between the band topology and nonlinear responses in topological materials.

Conclusion

In conclusion, by uncovering a violation of Ohm's law and the third-order Hall effect, we could identify the temperature at which a TPT occurs in ZrTe_5 . While a subtle change in the band topology is hidden in linear transport coefficients, it is detected by nonlinear conductivities due to the sensitivity of nonlinear transport to the band topology. In addition, we propose scaling relations for both linear and nonlinear transport coefficients, extending the existing scaling theory between linear transport coefficients. The microscopic mechanism for this generalized scaling theory is elusive at present, and thus, determining this mechanism is an interesting future problem to consider by taking into account the interplay between Berry curvature and disorder scattering. The role of disorder scattering in nonlinear transport coefficients has not been appropriately addressed, in which various geometrical objects²⁷ associated with the Berry curvature would affect the scaling relation. Even for a typical ferromagnetic metal, verifying the interplay between disorder scattering and Berry curvature in nonlinear transport coefficients remains an interesting future study.

Methods

Sample synthesis and characterization. The ZrTe_5 single crystals used in this study were grown by the Te-flux method. High-purity Zr and Te with an elemental ratio of $\text{Zr}_{0.0025}\text{Te}_{0.9975}$ were sealed under vacuum in a double-walled quartz ampoule. As the melting (T_m) and remelting (T_{rm}) temperatures are the main growth parameters during the flux method process, we explored their effects on the growth of the ZrTe_5 single crystal. They control the amount of Te deficiency, which determines the position of the Fermi energy as a dopant. We heated the sealed ampoules to T_m in a box furnace and left them at that temperature for 12 h to achieve homogeneity. The furnace was cooled to T_{rm} and further cooled to 420 °C in 60 h. The ZrTe_5 crystals were isolated from the Te flux by centrifugation at 420 °C. The flux-grown ZrTe_5 crystals had a needle shape with a typical size of approximately 1.20–5 mm in length and 0.01–0.23 mm in the other two dimensions. We systematically varied the melting temperature T_m between 900 °C and 1000 °C and the remelting temperature T_{rm} between 650 °C and 500 °C and grew thirteen high-quality ZrTe_5 single crystals. We thoroughly investigated the potential interference of trapped flux inclusions in our measurements by performing comprehensive Energy-Dispersive X-ray spectroscopy (EDX) mapping on our samples as shown in Supplementary Fig. 1. This process helped us assess the uniformity of the sample composition, thereby validating the optimal quality of ZrTe_5 . Our EDX results reveal that the atomic ratio of S11, S12, and S13 among thirteen single crystals are close to stoichiometry [Supplementary Table 1]. Hence, it is improbable that our findings

would be influenced by potential anomalies, such as trapped flux inclusions.

Transport measurements. Electrical and MR transport measurements of the ZrTe_5 single crystals were performed in a cryogen-free magnet system (Cryogenic, Inc.) from 1.7 to 300 K and from $B = -9$ T to $B = +9$ T using the six-probe method. In the longitudinal configuration, B and I were applied parallel in the ac -plane ($B \parallel I \parallel a$), while in the transverse configuration ($E \perp B$), B was applied along the b -axis ($B \parallel b$) and I in the ac -plane ($I \parallel a$). Those single crystals close to stoichiometry showed a pronounced negative LMR and a large anomalous effect. We conducted current-voltage measurements using a current source (Keithley 220) and a nanovoltmeter (Agilent 34420 A) to examine the signature of nonlinear electrical transport phenomena. Third harmonic signals in the Hall (transverse) channel were measured using lock-in amplifiers (NF Corporation LI 5640 and Stanford Research Systems SR830) with excitation frequencies between 77 Hz and 2177 Hz. A voltage-to-current converter (Stanford Research Systems CS580) supplied a sinusoidal current with a constant amplitude to the samples. We carefully monitored the temperature stability in all the experiments and successfully ruled out the heating effect as the origin of the nonlinear transport phenomena. We limited the applied current to below the value of a sudden slope change in the I - V curves when sample heating was induced. Additionally, we conducted additional measurements with a thermometer attached directly to the sample, providing real-time thermal data [Supplementary Fig. 4]. Furthermore, measurements were performed on the same sample with different distances between contacts [Supplementary Fig. 5], which provided further evidence to confirm the stability of the sample under the experimental conditions. This comprehensive approach has allowed us to convincingly rule out heating effects as a contributing factor to the nonlinear transport phenomena observed.

Next, we tackle the issue of establishing low-resistance contacts with these samples, a challenge that we met by adopting the methods outlined in the provided references, thus ensuring the quality of our contacts. We have gathered comprehensive evidence to validate the quality of our contacts, including measurements of contact resistance at 2 K, 2-point IV curves, as well as 4-point IV curves using voltage probes at varying contact distances measured on the same sample [Supplementary Fig. 6]. This evidence affirms our ability to maintain low-resistance contacts, a critical factor in our investigations.

Data availability

The data supporting the findings of this study are available upon reasonable request. This includes experimental and analytical data: • Access and Storage: Data is stored in secure, digital repositories and can be accessed by contacting the corresponding author. • Restrictions: There are no significant restrictions on data access, except for any data with privacy or confidentiality concerns. • Contact for Data Requests: [Heon-Jung Kim and hjkim76@daegu.ac.kr]. • No Published Repositories: There are no datasets in published repositories associated with this study. • No Data Generated Statement: Data sharing is not applicable as no datasets were generated or analyzed in this study.

Received: 15 April 2023; Accepted: 7 December 2023;

Published online: 20 December 2023

References

1. Wimmer, M., Price, H. M., Carusotto, I. & Peschel, U. Experimental measurement of the Berry curvature from anomalous transport. *Nat. Phys.* **13**, 545–550 (2017).
2. Liang, T. et al. Anomalous Hall effect in ZrTe_5 . *Nat. Phys.* **14**, 451–455 (2018).

3. Nagaosa, N., Sinova, J., Onoda, S., MacDonald, A. H. & Ong, N. P. Anomalous Hall effect. *Rev. Mod. Phys.* **82**, 1539 (2010).
4. Arnold, F. et al. Negative magnetoresistance without well-defined chirality in the Weyl semimetal TaP. *Nat. Commun.* **7**, 1–7 (2016).
5. Burkov, A. Negative longitudinal magnetoresistance in Dirac and Weyl metals. *Phys. Rev. B* **91**, 245157 (2015).
6. Son, D. & Spivak, B. Chiral anomaly and classical negative magnetoresistance of Weyl metals. *Phys. Rev. B* **88**, 104412 (2013).
7. Xiong, J. et al. Evidence for the chiral anomaly in the Dirac semimetal Na₃Bi. *Science* **350**, 413–416 (2015).
8. Zhang, C.-L. et al. Signatures of the Adler–Bell–Jackiw chiral anomaly in a Weyl fermion semimetal. *Nat. Commun.* **7**, 1–9 (2016).
9. Wang, Y. et al. Gate-tunable negative longitudinal magnetoresistance in the predicted type-II Weyl semimetal WTe₂. *Nat. Commun.* **7**, 1–6 (2016).
10. Shin, D. et al. Violation of Ohm’s law in a Weyl metal. *Nat. Mater.* **16**, 1096–1099 (2017).
11. Li, Q. et al. Chiral magnetic effect in ZrTe₅. *Nat. Phys.* **12**, 550–554 (2016).
12. Kim, H.-J. et al. Dirac versus Weyl fermions in topological insulators: Adler–Bell–Jackiw anomaly in transport phenomena. *Phys. Rev. Lett.* **111**, 246603 (2013).
13. Kim, P., Ryoo, J. H. & Park, C.-H. Breakdown of the chiral anomaly in Weyl semimetals in a strong magnetic field. *Phys. Rev. Lett.* **119**, 266401 (2017).
14. Huang, X. et al. Observation of the chiral-anomaly-induced negative magnetoresistance in 3D Weyl semimetal TaAs. *Phys. Rev. X* **5**, 031023 (2015).
15. Andreev, A. & Spivak, B. Longitudinal negative magnetoresistance and magnetotransport phenomena in conventional and topological conductors. *Phys. Rev. Lett.* **120**, 026601 (2018).
16. Dai, X., Du, Z. & Lu, H.-Z. Negative magnetoresistance without chiral anomaly in topological insulators. *Phys. Rev. Lett.* **119**, 166601 (2017).
17. Goswami, P., Pixley, J. & Sarma, S. D. Axial anomaly and longitudinal magnetoresistance of a generic three-dimensional metal. *Phys. Rev. B* **92**, 075205 (2015).
18. Gao, Y., Zhang, F. & Zhang, W. Second-order nonlinear Hall effect in Weyl semimetals. *Phys. Rev. B* **102**, 245116 (2020).
19. Gao, Y., Yang, S. A. & Niu, Q. Field induced positional shift of Bloch electrons and its dynamical implications. *Phys. Rev. Lett.* **112**, 166601 (2014).
20. Morimoto, T. & Nagaosa, N. Topological nature of nonlinear optical effects in solids. *Sci. Adv.* **2**, e1501524 (2016).
21. Morimoto, T., Zhong, S., Orenstein, J. & Moore, J. E. Semiclassical theory of nonlinear magneto-optical responses with applications to topological Dirac/Weyl semimetals. *Phys. Rev. B* **94**, 245121 (2016).
22. Sodemann, I. & Fu, L. Quantum nonlinear Hall effect induced by Berry curvature dipole in time-reversal invariant materials. *Phys. Rev. Lett.* **115**, 216806 (2015).
23. Xu, S.-Y. et al. Electrically switchable Berry curvature dipole in the monolayer topological insulator WTe₂. *Nat. Phys.* **14**, 900–906 (2018).
24. You, J.-S., Fang, S., Xu, S.-Y., Kaxiras, E. & Low, T. Berry curvature dipole current in the transition metal dichalcogenides family. *Phys. Rev. B* **98**, 121109 (2018).
25. Liu, H. et al. Berry connection polarizability tensor and third-order Hall effect. *Phys. Rev. B* **105**, 045118 (2022).
26. Lai, S. et al. Third-order nonlinear Hall effect induced by the Berry-connection polarizability tensor. *Nat. Nanotechnol.* **16**, 869–873 (2021).
27. Gianfrate, A. et al. Measurement of the quantum geometric tensor and of the anomalous Hall drift. *Nat* **578**, 381–385 (2020).
28. Li, Z. et al. Optical detection of quantum geometric tensor in intrinsic semiconductors. *Sci. China Phys. Mech.* **64**, 1–6 (2021).
29. Wang, Y. et al. Gigantic magnetochiral anisotropy in the topological semimetal ZrTe₅. *Phys. Rev. Lett.* **128**, 176602 (2022).
30. Zhang, Y. et al. Electronic evidence of temperature-induced Lifshitz transition and topological nature in ZrTe₅. *Nat. Commun.* **8**, 1–9 (2017).
31. Louvet, T., Houzet, M. & Carpentier, D. Signature of the chiral anomaly in ballistic Weyl junctions. *J. Phys. Mater.* **1**, 015008 (2018).
32. Matus, P., Dantas, R. M., Moessner, R. & Surówka, P. Skin effect as a probe of transport regimes in Weyl semimetals. *Proc. Natl Acad. Sci. USA* **119**, e2200367119 (2022).
33. Tang, F. et al. Three-dimensional quantum Hall effect and metal–insulator transition in ZrTe₅. *Nat* **569**, 537–541 (2019).
34. Tian, Y., Ghassemi, N. & Ross, J. H. Jr Gap-Opening Transition in Dirac Semimetal ZrTe₅. *Phys. Rev. Lett.* **126**, 236401 (2021).
35. Wang, J. et al. Vanishing quantum oscillations in Dirac semimetal ZrTe₅. *Proc. Natl Acad. Sci. USA* **115**, 9145–9150 (2018).
36. Chen, R. et al. Optical spectroscopy study of the three-dimensional Dirac semimetal ZrTe₅. *Phys. Rev. B* **92**, 075107 (2015).
37. Chen, R. et al. Magnetoinfrared spectroscopy of Landau levels and Zeeman splitting of three-dimensional massless Dirac fermions in ZrTe₅. *Phys. Rev. Lett.* **115**, 176404 (2015).
38. Zheng, G. et al. Transport evidence for the three-dimensional Dirac semimetal phase in ZrTe₅. *Phys. Rev. B* **93**, 115414 (2016).
39. Li, X.-B. et al. Experimental observation of topological edge states at the surface step edge of the topological insulator ZrTe₅. *Phys. Rev. Lett.* **116**, 176803 (2016).
40. Wu, R. et al. Evidence for topological edge states in a large energy gap near the step edges on the surface of ZrTe₅. *Phys. Rev. X* **6**, 021017 (2016).
41. Moreschini, L. et al. Nature and topology of the low-energy states in ZrTe₅. *Phys. Rev. B* **94**, 081101 (2016).
42. Manzoni, G. et al. Evidence for a strong topological insulator phase in ZrTe₅. *Phys. Rev. Lett.* **117**, 237601 (2016).
43. Manzoni, G. et al. Temperature dependent non-monotonic bands shift in ZrTe₅. *J Electron Spectros. Relat. Phenomena* **219**, 9–15 (2017).
44. Xu, B. et al. Temperature-driven topological phase transition and intermediate Dirac semimetal phase in ZrTe₅. *Phys. Rev. Lett.* **121**, 187401 (2018).
45. Tian, Y., Ghassemi, N. & Ross, J. H. Jr Dirac electron behavior and NMR evidence for topological band inversion in ZrTe₅. *Phys. Rev. B* **100**, 165149 (2019).
46. Liu, Y. et al. Zeeman splitting and dynamical mass generation in Dirac semimetal ZrTe₅. *Nat. Commun.* **7**, 1–9 (2016).
47. Sun, Z. et al. Large Zeeman splitting induced anomalous Hall effect in ZrTe₅. *npj Quantum Mater* **5**, 1–7 (2020).
48. Choi, Y., Villanova, J. W. & Park, K. Zeeman-splitting-induced topological nodal structure and anomalous Hall conductivity in ZrTe₅. *Phys. Rev. B* **101**, 035105 (2020).
49. Martino, E. et al. Two-dimensional conical dispersion in ZrTe₅ evidenced by optical spectroscopy. *Phys. Rev. Lett.* **122**, 217402 (2019).
50. Shahi, P. et al. Bipolar conduction as the possible origin of the electronic transition in pentatellurides: Metallic vs semiconducting behavior. *Phys. Rev. X* **8**, 021055 (2018).
51. Salzmann, B. et al. Nature of native atomic defects in ZrTe₅ and their impact on the low-energy electronic structure. *Phys. Rev. Mater.* **4**, 114201 (2020).
52. Salawu, Y. A., Yun, J. H., Rhyee, J.-S., Sasaki, M. & Kim, H.-J. Weak antilocalization, spin–orbit interaction, and phase coherence length of a Dirac semimetal Bi_{0.97}Sb_{0.03}. *Sci. Rep.* **12**, 1–10 (2022).
53. Vashist, A., Gopal, R. & Singh, Y. Anomalous negative longitudinal magnetoresistance and violation of Ohm’s law deep in the topological insulating regime in Bi_{1-x}Sb_x. *Sci. Rep.* **11**, 1–7 (2021).
54. Kim, K.-S., Kim, H.-J. & Sasaki, M. Boltzmann equation approach to anomalous transport in a Weyl metal. *Phys. Rev. B* **89**, 195137 (2014).
55. Duan, J. et al. Giant second-order nonlinear Hall effect in twisted bilayer graphene. *Phys. Rev. Lett.* **129**, 186801 (2022).
56. Du, Z., Lu, H.-Z. & Xie, X. Nonlinear Hall effects. *Nat. Rev. Phys.* **3**, 744–752 (2021).
57. Pacchioni, G. The Hall effect goes nonlinear. *Nat. Rev. Phys.* **4**, 514–514 (2019).
58. Iguchi, S., Hanasaki, N. & Tokura, Y. Scaling of anomalous hall resistivity in Nd₂(Mo_{1-x}Nb_x)₂O₇ with spin chirality. *Phys. Rev. Lett.* **99**, 077202 (2007).
59. Miyasato, T. et al. Crossover behavior of the anomalous Hall effect and anomalous Nernst effect in itinerant ferromagnets. *Phys. Rev. Lett.* **99**, 086602 (2007).
60. Liu, E. et al. Giant anomalous Hall effect in a ferromagnetic kagome-lattice semimetal. *Nat. Phys.* **14**, 1125–1131 (2018).
61. Haldane, F. Berry curvature on the fermi surface: Anomalous Hall effect as a topological fermi-liquid property. *Phys. Rev. Lett.* **93**, 206602 (2004).
62. Wang, Y. et al. Nonlinear transport due to magnetic-field-induced flat bands in the nodal-line semimetal ZrTe₅. *Phys. Rev. Lett.* **131**, 146602 (2023).
63. Wang, W. et al. Evidence for layered quantized transport in Dirac semimetal ZrTe₅. *Sci. Rep.* **8**, 1–5 (2018).
64. Nakatsuji, S., Kiyohara, N. & Higo, T. Large anomalous Hall effect in a non-collinear antiferromagnet at room temperature. *Nat* **527**, 212–215 (2015).
65. Nayak, A. K. et al. Large anomalous Hall effect driven by a nonvanishing Berry curvature in the noncollinear antiferromagnet Mn₃Ge. *Sci. Adv.* **2**, e1501870 (2016).
66. Yang, S.-Y. et al. Giant, unconventional anomalous Hall effect in the metallic frustrated magnet candidate, KV₃Sb₅. *Sci. Adv.* **6**, eabb6003 (2020).

Acknowledgements

This research was supported by the Basic Science Research Program through the National Research Foundation of Korea (NRF) funded by the Ministry of Science, ICT & Future Planning (2021R1A2C2005162 and 2021R1A4A3029839).

Author contributions

H.-J.K. conceived the main idea of the experiment. Y.A.S. conducted all the experiments. Y.A.S., H.-J.K., J.H.K., J.-S.R., and K.-S.K. analysed the experimental data. Y.A.S., D.A., J.H.K., and M.S. grew the single crystals. H.-J.K., K.-S.K., and Y.A.S. prepared the manuscript, incorporating the comments from all the other co-authors.

Competing interests

The authors declare no competing interests.

Additional information

Supplementary information The online version contains supplementary material available at <https://doi.org/10.1038/s43246-023-00437-5>.

Correspondence and requests for materials should be addressed to Ki-Seok Kim or Heon-Jung Kim.

Peer review information *Communications Materials* thanks the anonymous reviewers for their contribution to the peer review of this work. Primary Handling Editor: Aldo Isidori. A peer review file is available.

Reprints and permission information is available at <http://www.nature.com/reprints>

Publisher's note Springer Nature remains neutral with regard to jurisdictional claims in published maps and institutional affiliations.



Open Access This article is licensed under a Creative Commons Attribution 4.0 International License, which permits use, sharing, adaptation, distribution and reproduction in any medium or format, as long as you give appropriate credit to the original author(s) and the source, provide a link to the Creative Commons license, and indicate if changes were made. The images or other third party material in this article are included in the article's Creative Commons license, unless indicated otherwise in a credit line to the material. If material is not included in the article's Creative Commons license and your intended use is not permitted by statutory regulation or exceeds the permitted use, you will need to obtain permission directly from the copyright holder. To view a copy of this license, visit <http://creativecommons.org/licenses/by/4.0/>.

© The Author(s) 2023